metals

MDPI

Article

Microstructural and Oxidation Effects of Nb Additions to U_3Si_2

Geronimo Robles [1,2,*], Joshua T. White [2], Scarlett Widgeon Paisner [2] and Elizabeth S. Sooby [1]

[1] Department of Physics and Astronomy, University of Texas at San Antonio, One UTSA Circle, San Antonio, TX 78249, USA; elizabeth.sooby@utsa.edu
[2] Los Alamos National Laboratory, P.O. Box 1663, Los Alamos, NM 87545, USA; jtwhite@lanl.gov (J.T.W.); scarlettw@lanl.gov (S.W.P.)
* Correspondence: geronimo.robles@utsa.edu; Tel.: +1-210-725-1947

Abstract: U_3Si_2 is a long term, accident-tolerant nuclear fuel candidate for light-water reactors because of its superior thermal conductivity and increased uranium density when compared to traditional uranium dioxide (UO_2). While reducing internal thermal stresses and increasing efficiency, U_3Si_2 exhibits energetic oxidation during certain off-normal and accident scenarios, which include coolant or steam exposure. To mitigate this, Nb is investigated as an alloy constituent to enhance corrosion resistance and increase mechanical strength. The work presented investigates the response of Nb-alloyed U_3Si_2 to steam atmospheres. A thermogravimetric analysis is conducted in flowing steam to T > 1000 °C to assess oxidation resistance. The phase characterization of as-melted, thermally annealed and post-oxidation compositions with up to 12 vol% Nb by powder X-ray diffraction, scanning electron microscopy, and energy dispersive spectroscopy is reported.

Keywords: high-temperature nuclear fuel synthesis; high-temperature oxidation; high-uranium-density nuclear fuel; accident-tolerant nuclear fuel

Citation: Robles, G.; White, J.T.; Widgeon Paisner, S.; Sooby, E.S. Microstructural and Oxidation Effects of Nb Additions to U_3Si_2. *Metals* **2024**, *14*, 1239. https://doi.org/10.3390/met14111239

Academic Editor: Hélder Puga, Rongshan Qin, Oleg Mishin, Heinz-Günter Brokmeier

Received: 30 September 2024
Revised: 23 October 2024
Accepted: 25 October 2024
Published: 30 October 2024

1. Introduction

Accident-tolerant fuels to replace the current uranium dioxide (UO_2) fuel form in light-water reactors (LWRs) have been the focus of recent research [1–13]. In particular, the development of uranium silicide fuel candidates has been at the forefront of this research because of their high uranium density and improved thermal conductivity when compared to UO_2 [3,6,9,14,15]. These thermophysical properties decrease the thermal gradient across the fuel pellet, reducing stress while also improving the power to melt. Suitable replacements of UO_2 in LWR scenarios should not displace the fissile loading, which limits the available U-Si binary compounds to U_3Si and U_3Si_2. U_3Si and U_3Si_2 maintain a uranium density greater than UO_2 (9.75 gU/cm^3). The highest uranium density candidate, U_3Si with 14.7 gU/cm^3, has been deployed in low-temperature research reactors but is not considered for LWR deployment due to instabilities like disordering and swelling at temperatures of the current LWR fleet [16–18]. Further, U_3Si_2 is not projected to perform well in some relevant design-basis and beyond design-basis accidents or scenarios as a pure, single phase fuel [14,19].

U_3Si_2 is a line compound which maintains a single crystal structure from room temperature to 1640 °C [15,20], and its uranium density is 16.5% higher than UO_2 at 11.3 gU/cm^3. In the literature, an improved delay of oxidation onset temperature has been achieved by alloys [14,21], composites [5,6,22–25], and microstructural control [3,21,26]. The work presented here aligns with the alloy concept and investigates the addition of the Nb metal to the U_3Si_2 fuel form at volume percents below 12%. Nb additions are considered in this work, as these additions have provided oxidation and chemical resistance in other high-temperature applications, such as aerospace engineering and chemical handling, and are proposed here to mitigate the waterside corrosion of U_3Si_2 [27,28]. Historically, Nb received attention for application in nuclear reactors due to its low-thermal neutron-absorption

cross-section, high-temperature mechanical properties, and good fabricability in cast and powder metallurgical processes [27–29]. To be considered for drop-in replacement, the concentration of Nb added should not offset the fissile loading below UO_2 at 9.75 gU/cm^3 [15]. The Nb content for each composition studied here was calculated using the Rule of Mixtures (ROM) as detailed in [14], such that the uranium density of the alloy would be greater than or equal to that of UO_2.

The available literature on the U-Si-Nb ternary system is limited to one study conducted by Lebihan et al. [29]. The chosen compositions in the Lebihan study were arc-melted and then annealed, one at 850 °C and the other at 1000 °C. The annealing treatments revealed two ternary compositions in their respective isothermal sections of the ternary U-Si-Nb system. $U_2Nb_3Si_4$ and $U_{(2-x)}Nb_{(3+x)}Si_4$ formed as plates or needles in two-phase equilibrium at 1000 °C. From this, it was inferred that these ternary compounds are thermodynamically stable [29]. At 850 °C, a single U-Nb-Si phase, $U_2Nb_3Si_4$, formed in equilibrium with both U_3Si_2 and USi showing no Nb solubility. The U-rich phase $U_{99.3}Nb_{0.6}Si_{0.2}$ was also identified, showing very low solubility of Nb and Si [29]. However, these ternaries ranged from 32.2 wt% Nb ($U_2Nb_3Si_4$) to 37.4 wt% Nb ($U_{19.3}Nb_{37.4}Si_{43.3}$), which are far from the 8.7 wt% (12 vol%) Nb of the highest stoichiometry resultant of the low-volume-percent Nb-concentration additions fabricated here.

In this work, volume percent additions of Nb to U_3Si_2 are investigated as a method for delaying the oxidation onset temperature of the fuel in atmospheres beyond what is expected for normal reactor operation (T∼700 °C) as well as off-normal and accident scenarios (T>∼1000 °C). To characterize this behavior, the samples are fabricated by arc melting and subjected to high-temperature steam oxidation testing to assess the impact of Nb on oxidation resistance. The compositions are characterized by SEM/EDS and XRD at each step to detail phase and microstructural evolution. The results are discussed in relation to U_3Si_2 oxidation performance and compared to other alloying elements and composite designs under consideration for LWR deployment. This suite of experiments comprises a type of quick screening test for determining if a fuel concept should be investigated further.

2. Materials and Methods

2.1. Sample Fabrication

U_3Si_2 feedstock was fabricated from depleted uranium (U) sourced from AeroJet Rocketdyne (Jonesborough, TN, USA) and pure silicon (Si) beads (Alfa Aesar, 99.999% metals basis) or silicon chunks (Cerac, 99.999% metals basis). U was stored inside an Ar atmosphere MBraun glovebox maintained at partial pressures of O_2 (pO_2) and H_2O (pH_2O) less than 0.1 part per million (ppm). Metal U cylinders (>12 g) were segmented into multiple pieces (<5 g) by an abrasive cut-off wheel. The remaining surface oxide was removed by mechanical grinding until the metal showed a bright shiny silver finish. After cleaning with methanol, the U pieces were weighed on a Mettler-Toledo balance calibrated to 0.0001 g inside the glovebox. Before the U metal was transferred to the arc melter, the final mass of each piece was recorded and used to calculate the mass of Si needed to achieve stoichiometric U_3Si_2. Although Wagner et al. demonstrated the synthesis of phase-pure U_3Si_2 from stoichiometric amounts of U and Si through arc melting, it was determined that for this study, the incorporation of excess Si would yield an ingot with the correct final mass. We found through methodological optimization and trial synthesis that the optimum total weight size is near 5 g. Up to 1 wt% of excess Si was included as it was expected that Si would volatilize preferentially to U due to the difference in vapor pressure for the pure metals at melting temperature [9]. Immediately before each charge was melted, the U and Si quantities were ultra-sonicated for 10 min each in acetone and then methanol. U and Si were combined, via a Centorr Vacuum Industries TriArc furnace customized with power supplies, to each of the three electrodes and active cooling to the hearth. Ar supply gas to the furnace was gettered before entering the furnace chamber. An additional internal titanium getter charge was deployed throughout the melting procedure to maintain chamber O_2 levels below 10^{-15} ppm. Melting began with a consolidation of the pure metals,

which were then flipped, melted, and cooled at least five times to encourage homogeneity. Post-melt masses were recorded to check mass loss due to volatilization. U_3Si_2 ingots were cataloged and stored in Ar gloveboxes. Final U_3Si_2 ingot masses were compared with the theoretical masses expected from stoichiometric calculations. No more than 0.5 wt% mass difference ($<\sim$25 mg) from the calculated theoretical mass was allowed. was allowed; ingot masses with differences not more than a 10 mg loss were used in this study. Ingots synthesized by the same method as part of a different study were characterized and shown to be free of secondary phases.

Fabrication of the target Nb-bearing compositions began with the mechanical fracturing of the U_3Si_2 bulk material in the glovebox. Ingot sizes of the U-Si-Nb compositions were chosen to be within 2 to 3 g for ease of synthesis and minimization of the loss of volatile species at high temperature. The amount of Nb required to achieve U_3Si_2+ (0.5, 1.0, 2.00, 2.67, 6.67, and 11.88) vol% Nb was calculated via the Rule Of Mixtures approximation (ROM) as described in Sooby Wood et al. and shown here in Equations (1) and (2) [14]. Equation (1) was used to determine a theoretical density. From there, the mass fraction of Nb required per mass of U_3Si_2 could be obtained by Equation (2). Excess Nb was not added to the initial U-Si melt because of its vapor pressure and melt temperature, which indicate a low probability of volatilization. Segmenting, cleaning, and weighing of a Nb wire (Beantown Chemical, 99.99% metals basis) was conducted on the benchtop and loaded into the arc melt furnace. The incorporation of Nb into U_3Si_2 was completed via the arc melt process outlined above.

$$[\rho(X) \times Vol\%(X)] + [\rho(U_3Si_2) \times Vol\%(U_3Si_2)] = \rho(ROM) \quad (1)$$

$$\frac{\rho(X)}{\rho(ROM)} \times Vol\%(X) = X_{MassFraction} \quad (2)$$

2.2. Microstructural Analysis

Phase identification and qualitative analysis began with the imaging of a sample cross-section representative of each composition. In the Ar glovebox, each Nb-bearing ingot was fractured by mortar and pestle and a representative fragment was chosen from nearest to the center of the ingot. Fragments were mounted in epoxy pucks, mechanically ground, and then polished. A final 0.5 µm finish was achieved on Allied Hi-Tech Vel-Cloth and 0.5 µm polycrystaline diamond suspension fluid in preparation for scanning electron microscopy (SEM). The Hitachi FlexSEM 1000 SEM, equipped with an energy dispersive spectroscopy (EDS) detector, was used to collect images in both secondary electron (SE) and backscattered electron (BSE) modes. EDS analysis was completed with the AZtecOne ver. 4.3 (Oxford Instruments) software suite.

Powder X-ray diffraction (XRD) measurements were performed in a Bruker D2-Phaser benchtop diffractometer. Powders were prepared in the glovebox by manual grinding and then loaded into an O-ring sealed, polymer-domed sample holder to minimize oxidation during transfer to the benchtop diffractometer. Measurements were taken from 10 to 90° 2θ at a 0.01° step and 1 s dwell time. The initial phase identification and qualification were conducted via Diffrac.EVA software interfaced with the ICDD PDF-2 database.

2.3. Heat Treatment

Despite the flipping and re-melting steps included in the arc melting procedure, rapid cooling at the end of melting can lead to metastable phase segregation with subsequent inhomogeneous phase composition and distribution. The extensive time commonly required to achieve equilibrium in these materials, if possible, is not conducive to the arc melting process. Two separate heat treatment processes were performed by producing two different sample sets (as fabricated and annealed). Fragments treated in an air-atmosphere benchtop Thermcraft XSB furnace were individually wrapped in a tantalum, marked, and sealed inside a stainless-steel ConFlat assembly (Kurt J. Lesker, CF40). Packaging of the assembly took place inside the Ar glovebox to preserve an inert internal atmosphere. The U_3Si_2 +

11.88 vol% Nb composition was ramped at 10 °C·min^{-1} to 725 °C and held for 100 h as it was packaged with other low-melt materials. The remaining compositions were similarly packaged for heat treatment in a flow-through Ar atmosphere benchtop Carbolite-Gero tube furnace (model EST 12/300B), which ramped at 10 °C·min^{-1} to 950 °C and held for 200 h. Pure titanium and zirconium ingots were deployed as getters within the flow of argon to maintain O_2 levels below 10^{-15} ppm. All compositions cooled to room temperature and were returned to the Ar glovebox for disassembly. No oxidation was observed following heat treatment.

2.4. Steam Oxidation Testing

Steam exposures were carried out in a Netzsch Instruments' simultaneous thermal analyzer (STA 449 F3 Jupiter, NETZSCH Analyzing & Testing, Selb, Germany) equipped with a water vapor furnace and generator (DV2ML, Astream). Fuel fragments of each composition were recorded and loaded into the STA to measure mass change as a function of temperature and time. Furnace fixturing, including the working tube and sample carrier, were Al_2O_3. Oxygen content of the STA inlet and outlet was recorded via an inline sensor system (RapidOx OEM 447, Cambridge Sensotec, St. Ives, UK) identical to those in the arc melt and heat treatment stages.

Samples were loaded into the STA and furnace atmosphere purged of residual air until the outlet was less than 10^{-15} ppm O_2. Each sample was then thermally ramped to 1000 °C, held for 30 min, and cooled at 20 °C per min. This method emulates previous work which examined onset temperatures of U-Si and U_3Si_2 + X compounds to allow for a direct comparison [14] Thermogravimetric measurements were terminated if a rapid mass loss of >2 mg in <30 s was detected, indicating an ejection of the material from the test crucible, similar to previous U_3Si_2 studies [14,19,30].

Determination of the oxidation onset temperature was conducted in Netzsch Proteus software v8.0. The integrated curve evaluation "onset" function was used and compared to the first derivative result of the thermogravimetric curve. This technique reproduces the c-DTA evaluation method that was covered in the review by Gonzales et al. [14]. A baseline correction measurement was acquired for each atmosphere and incorporated into analysis within the Netzsch software ver. 6. Phase identification of the resulting material was conducted with XRD to verify the end oxidation state.

Sample fragments were chosen from the as-fabricated or annealed ingot center and in the range of 75 to 150 mg. Samples were ramped at 10 °C/min in pure Ar with protective flow at 50 sccm and purge flow at 20 sccm. Thermal holds of 10 min at 200 and 300 °C were performed to dry and equilibrate the system. Once equilibrated, steam was produced at 7 g/h and transferred to the furnace with 8 NL/h of gettered Ar after 300 °C to prevent condensation. Thermal ramp continued at 10 °C/min, with a total partial pressure of steam (pH_2O) of 0.345 atm until the maximum 1117 °C setpoint. The dwell temperature of 1117 °C was maintained for 30 min, after which steam was removed, and the furnace cooled naturally to room temperature. An Al_2O_3 pedestal fixture was chosen for this exposure to allow for uninhibited sample reactivity with atmosphere, following Sooby Wood et al.'s work on the effect of fixturing geometry in flowing steam oxidation testing [14].

3. Results

3.1. Microstructural and Phase Characterization

The following results summarize the microstructural evolution between as-fabricated and heat-treated compositions and respective oxidation response. For each, phases are identified via XRD and SEM to quantify any changes to the composition as the concentration of Nb increased.

3.1.1. Characterization of as-Fabricated U-Si-Nb Ingots

Fragments from as-fabricated ingots were selected for XRD and SEM based on their location within the ingots. The pieces nearest to the center of the ingot's cross-section were

expected to be the least effected by non-equilibrium phase segregation from rapid cooling at the end of the arc melting process. The XRD analysis of the arc-melted buttons is shown in Figure 1, which identifies secondary U-Si and U-Si-Nb phases distributed in a U_3Si_2 matrix. For compositions below 3 vol% Nb, XRD patterns display little to no change in the the U_3Si_2 pattern or evidence of secondary phases, despite those phases being observed in SEM analysis. Lebihan et al. reported a thermodynamically stable ternary, $U_2Nb_3Si_4$, with a second, off-stoichiometric phase, $U_{2-x}Nb_{3+x}Si_4$, and also found negligible solid solubilities of Nb in the U_3Si_2 phase [29]. Figure 1 shows that ternary characteristic peaks at 29.2°, 35.3°, 36.8°, 39.2°, and 40.9° 2θ agree with new peak formations in the XRD patterns beginning, most notably, at 6.67 vol% Nb. However, a variation in the U_3Si_2 phase is evidenced by the peak intensity change and broadening as well as a 2θ shift in angle.

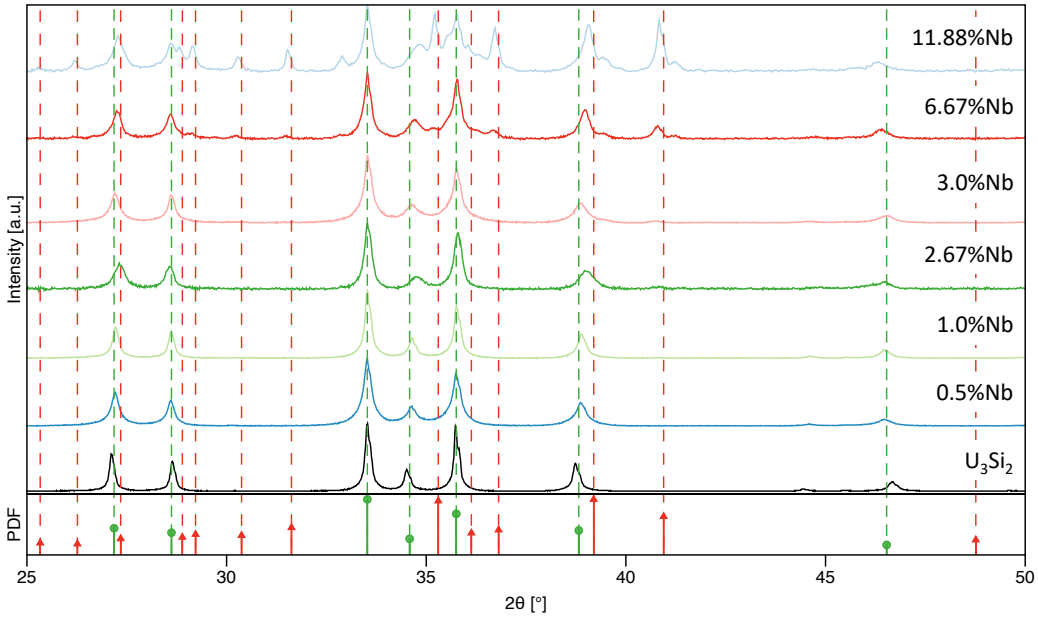

Figure 1. Comparison of all as-melted compositions of U_3Si_2 + Nb (increasing Nb concentration from bottom to top) with pure U_3Si_2 (bottom) and reference patterns for U_3Si_2 (green circles, 01-075-1941) and $U_2Nb_3Si_4$ (red triangle, 04-018-5866). Peaks less than a 10% relative intensity from these two reference patterns were excluded to promote clarity.

The primary U_3Si_2 phase shows peak broadening at the triplet located between 33° and 37° 2θ and shifting at both high and low angles. It is suspected that this shifting is evidence of Nb alloying into U_3Si_2 as reported by Lebihan et al. [29], and the broadening may indicate localized stresses induced by the high rates of heating and cooling during the arc melting process. However, a detailed crystallographic study to evaluate stresses within the lattice was not conducted as part of this investigation [29]. Lastly, UO_2 was not observed in the as-fabricated ingot's XRD patterns [19,20,29].

SEM micrographs collected in backscattered electron mode are shown in Figure 2 and present the as-fabricated U_3Si_2 + Nb alloys with the Nb concentration increasing from Figure 2A–F. Figure 2F presents each identified phase that is numerically labeled: (1) U_3Si_2 matrix, (2) $U_2Nb_3Si_4$, (3) a U-Si-Nb ternary rich in U, and (4) U-Si eutectic binary rich in U. The phases identified are consistent across all samples and omitted from Figure2A–E for clarity. The presence of a dark phase in Figure 2A indicates a Nb-bearing compound, which is expected to be below the detection limit of the XRD ($<\sim$ 0.5 wt%). The low-Nb-concentration samples (up to 3.0 vol% Nb) are shown in Figure 2A–D, which exhibit similar microstructural features, namely a low abundance of secondary phase (U-Si-Nb and U-Si eutectic type) distributed in a dominant U_3Si_2 matrix phase. In Figure 2A, the as-melted composition for the 0.5 vol% Nb addition shows three phases. Initial EDS measurements gave suggested that the brightest phase is the uranium–silicon eutectic near 91 at% U. The

darkest phase is identified as an off-stoichiometric ternary, and the intermediate gray phase is the U_3Si_2 matrix. In Figure 2B, the percent abundance of the U-Si eutectic and $U_2Nb_3Si_4$ phase increases while U_3Si_2 decreases. For compositions in Figure 2C,D, the presence of the U-Si eutectic is substantially decreased while abundances in $U_2Nb_3Si_4$ increase.

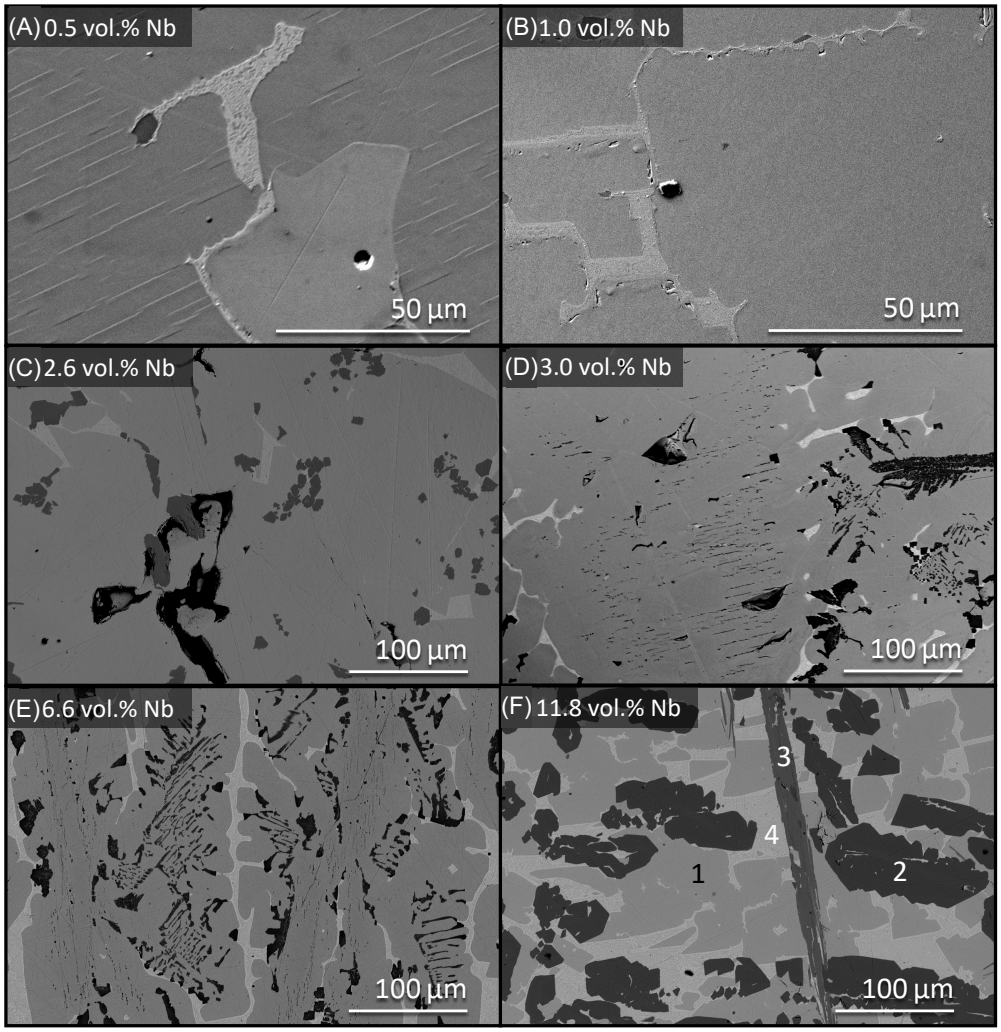

Figure 2. SEM micrographs of each as-fabricated ingot. The concentration of Nb increases from 0.5 vol% to 11.88 vol% in (**A**–**F**), respectively, as is labeled in each micrograph. As concentration increases, secondary phases distributed in U_3Si_2 increase. In (**F**), each individual phase is numbered: (1) U_3Si_2 matrix, (2) $U_2Nb_3Si_4$, (3) a U-Si-Nb ternary rich in U, and (4) U-Si eutectic binary. This labeling can be applied to images in (**A**–**E**).

Similarly, compositions with high concentrations of Nb (>3.0 vol% Nb) are shown in Figure 2E,F. The microstructure of the 6.67 vol% Nb alloy in Figure 2E shows that the abundance of U_3Si_2 decreases even more dramatically with an increase in $U_2Nb_3Si_4$. Finally, the highest concentration of Nb, 11.88 vol%, shows the development of an additional U-Nb-Si phase. In the images, the U-Si-Nb phase is visually distinguishable as a dark globular phase, with a Nb abundance of 30 wt%, and a plate-like phase possibly composed of other internal ternary phases. Figure 2F shows the microstructure of the 11.88 vol% Nb sample, including labels for each representative phase tabulated in Table 1. Here, phases 2, 3, and 4 are distributed in a medium-gray phase, 1, identified as U_3Si_2. Table 1 reports the change in phase abundances as Nb increases as a function of area as analyzed by ImageJ. It is noteworthy to mention that although images were processed in ImageJ, it is still possible that threshold bounds may have included portions of one phase as another. However,

an error of not more than 1% occurred over the triplicate measurements conducted on each image.

Table 1. Comparison of phases present and their respective abundances as measured from SEM images and tabulated via ImageJ software ver. 13.0.6.

Nb. Conc.	$\%U_3Si_2$ Phase 1		$\%U_2Nb_3Si_4$ Phase 2		%U-Si Eut. [1] Phase 3		$\%U_3Si$ Phase 4		$\%U_{1.75}Nb_{3.25}Si_4$ Phase 5	
	As-Fab	Ann	As-Fab	Ann	As-Fab	Ann	As-Fab	Ann	As-Fab	Ann
0.5%	93.70	92.31	0.30	2.69	6.00	0.00	0.00	6.00	0.00	0.00
1.0%	92.77	94.29	2.49	5.71	5.03	0.00	0.00	0.00	0.00	0.00
2.6%	94.48	87.50	4.59	5.82	1.00	7.44	0.00	0.00	0.00	0.00
3.0%	92.00	76.76	6.26	15.47	1.74	4.39	0.00	2.42	0.00	0.00
6.6%	79.81	64.50	10.17	11.87	10.02	12.34	0.00	8.70	0.00	0.00
11.88%	48.63	17.76	28.49	37.76	16.42	40.84	0.00	0.00	6.45	4.95

[1] Consulting the uranium–silicon binary phase diagram by Okamoto et al. [20], the eutectic identified here most closely matches 91 at% U-Si, which melts at 985 °C.

3.1.2. Characterization of annealed U-Si-Nb ingots

Figure 3 plots XRD patterns of all heat-treated compositions and confirms secondary U-Si and U-Si-Nb phases distributed within the dominant U_3Si_2 phase. In their annealed state, the ternary $U_2Nb_3Si_4$ is identified in every composition by characteristic peaks located at 29.2°, 35.3°, 36.8°, 39.2°, and 40.9° 2θ. A second ternary is identified at concentrations of 6.67% Nb and above by characteristic peaks at 35.9°, 35.6°, 29.7°, and 41.3° 2θ. Variation in the U_3Si_2 signature is observed as the peak shifting to a higher angle below 30° and above 37° 2θ. However, peak shifting was less evident than in the as-fabricated samples, which is attributed to a potentially lower intergranular strain because of reduced secondary phases. For the 0.5, 1.0, 2.6, and 3.0 vol% Nb compositions, the phases $U_2Nb_3Si_4$ and $U_{1.75}Nb_{3.25}Si_4$ were identified. At the 6.6 and 11.8 vol% Nb concentrations, the ratio of secondary phases to U_3Si_2 increases.

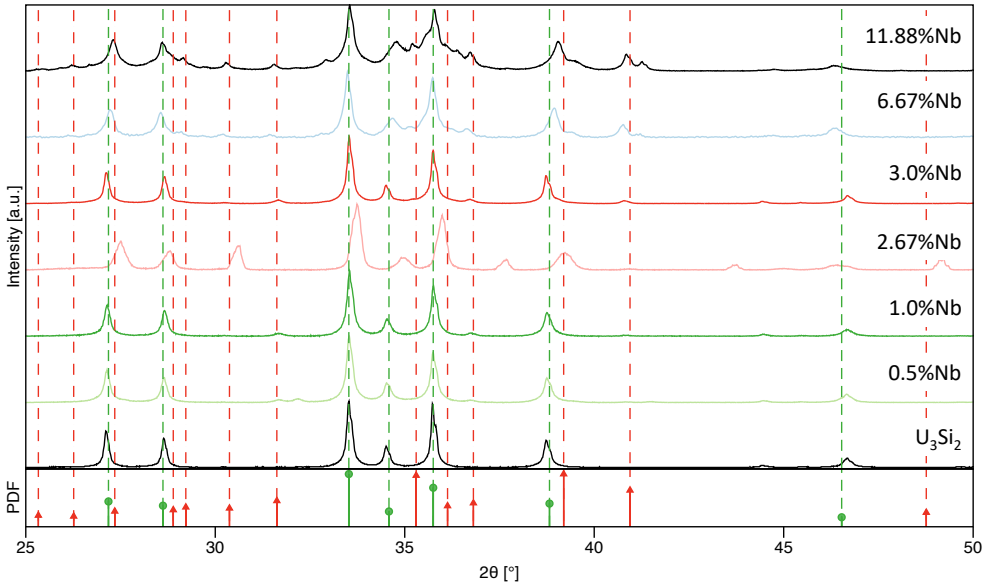

Figure 3. XRD pattern comparison of all annealed compositions of U_3Si_2 + Nb. Increasing Nb concentration (from bottom to top) with pure U_3Si_2 (bottom) and reference patterns for U_3Si_2 (green circles, 01-075-1941) and $U_2Nb_3Si_4$ (red triangle, 04-018-5866). Peaks less with than 10% relative intensities from these two reference patterns were excluded to promote clarity. Contaminant phases such as UO_2 are not present.

The SEM characterization of the annealed samples is presented in Figure 4. The images agree with the XRD analysis, wherein 0.5 and 1.0 vol% Nb concentrations showed a redistribution of the 91 at% U-Si eutectic phase such that a single $U_2Nb_3Si_4$ phase is homogeneously distributed in a U_3Si_2 matrix. At 2.6 and 3.0 vol% Nb, a bright U-rich phase remains, which is identified as most closely matching the U-rich eutectic. However, at 3.0 vol% Nb, the eutectic phase is surrounded by an additional secondary phase, 75 at% U; this phase is identified as U_3Si.

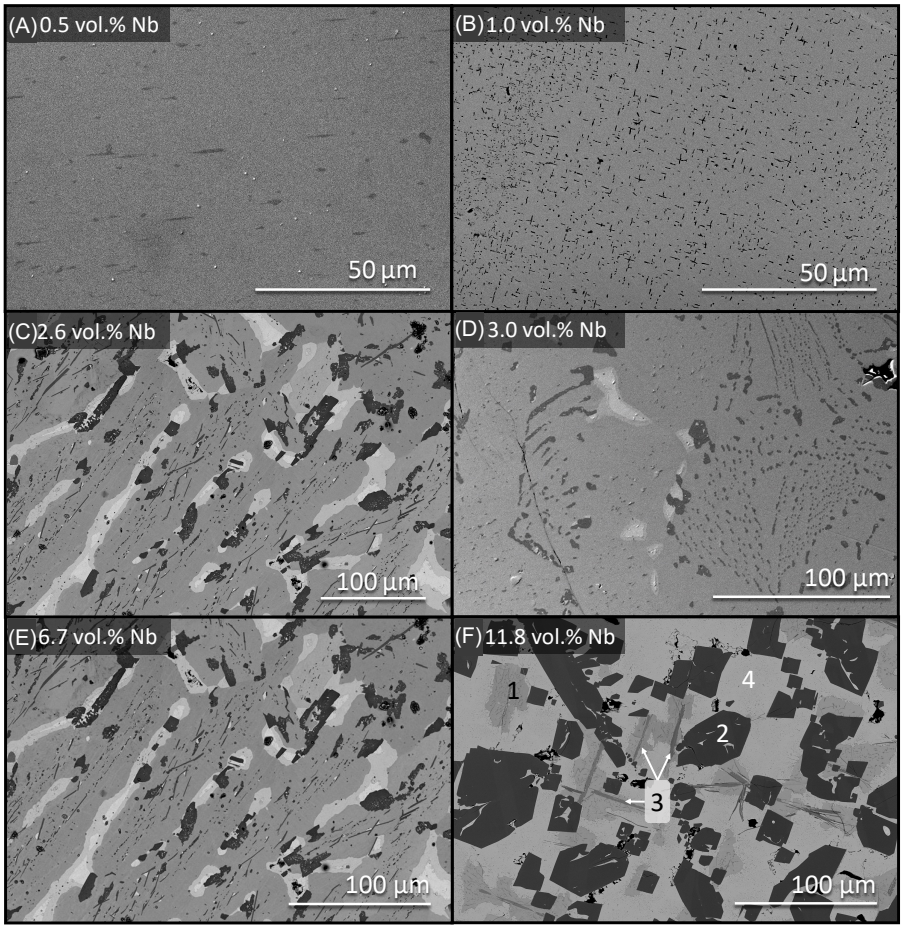

Figure 4. Backscatter SEM images of each U_3Si_2 + Nb composition increasing in concentration from (**A**–**F**). As Nb concentration increases, both the number of secondary phases distributed in U_3Si_2 and the relative fraction of secondary phases increase. In (**F**), each individual phase is numbered: (1) U_3Si_2 matrix, (2) $U_2Nb_3Si_4$, (3) a U-Si-Nb ternary rich in U, and (4) U-Si eutectic binary. The labled phases are consistent across the rest of the micrographs in this figure.

Nb concentrations of 6.6 and 11.8% are found to present the highest abundances of U-rich binary and U-Si-Nb ternary phases. Although the number of phases present in these concentrations do not change, a redistribution in the abundances is observed. U-rich phases such as U_3Si and the U eutectic, $U_2Nb_3Si_4$ and $U_{1.75}Nb_{3.25}Si_4$, increase while the total abundance of the matrix phase, U_3Si_2, is reduced to a greater degree than the as-fabricated samples. A summary of changes in the abundances of phases is reported in Table 1.

3.2. Thermogravimetric Analysis

In this section, the response of U_3Si_2 alloyed with Nb in the atmospheres and thermal profiles discussed in Section 2.4 is presented via thermograms. These plots show mass change as a function of temperature.

Oxidation in Steam

Figure 5 presents thermograms of all as-fabricated U_3Si_2 + Nb compositions. The thermogravimetric results are broken into distinct groups: arrested and completed. Arrested measurements demonstrated a large mass-loss event indicated by an abrupt change in the thermogravimetric curve in Figure 5A. Completed measurements are shown in Figure 5B. The onset temperature of U_3Si_2 is indicated throughout. Pure U_3Si_2 stock from this study was oxidized under identical conditions and its onset of oxidation temperature was calculated to be 409 °C. This result was ±25 °C from the published temperatures and, because of potential experimental variance, was used as the pure U_3Si_2 onset temperature [14]. The highest onset temperature observed for the arrested compositions occurred at 502.3 °C for the 2.6 vol% Nb. Despite achieving the highest delay temperature, 2.6, the 1.0 and 0.5 vol% Nb additions behaved the most like pure U_3Si_2 and required early termination of the experiment (Figure 5).

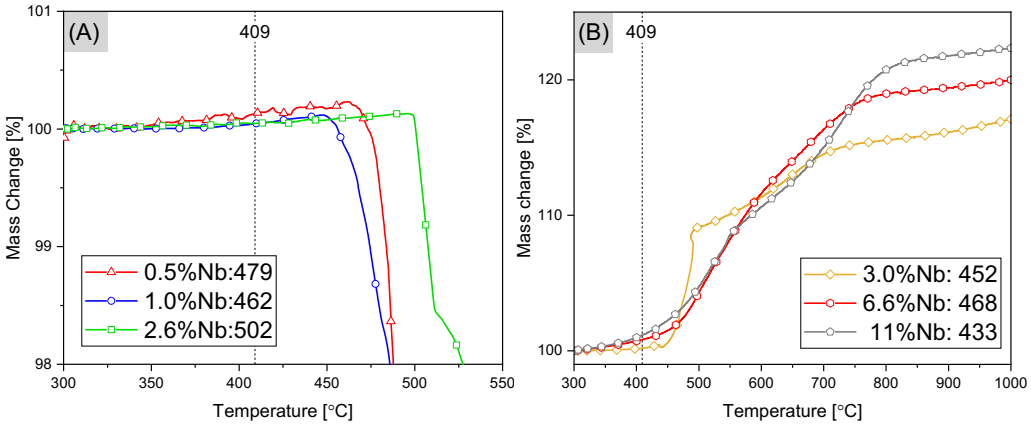

Figure 5. Thermogravimetric plots of all as-fabricated compositions oxidized in steam and ramped to 1000 °C. In each plot, the composition is labeled by its respective vol % Nb concentration and its oxidation onset temperature. I.e.: the U_3Si_2 + 0.5 vol% Nb composition is the red trend with triangle points and had an onset temperature of 479 °C. (**A**) Arrested measurements; (**B**) Completed measurements.

Compositions with Nb concentrations greater than 3.0 vol% did not experience a mass-loss event during the entire thermal ramp experiment. Of these, the 3.0% Nb showed the least amount of mass gain at 15% with an onset of oxidation at 452 °C while the 6.6% Nb had the highest onset temperature delay at 468 °C and a 19% mass gain. Despite observable improvements to onset temperature delay, the trend of total mass gain also increased as the concentration of Nb increased. However, the total mass gain of these composites remained less than the maximum theoretical mass gain of 25% for pure U_3Si_2 [14]. This could be partially attributed to the oxidation of Nb; however, Nb_2O_5 or other Nb oxides were not measured in any of the characterization techniques. It was determined that despite a lower onset temperature, the best performing composition was 3.0 vol% Nb.

Thermogravimetric measurements were completed for select annealed compositions and are shown in Figure 6 in the same manner as previously. Arrested measurements in Figure 6A are the low Nb concentrations; 0.5 and 1.0 vol% Nb. Completed annealed compositions include 3.0 and 11 vol% Nb and are shown in Figure 6B. All annealed compositions demonstrated an onset temperature delay of less than 460 °C. The lower onset temperature was accompanied by a total mass gain similar to the as-fabricated compositions, beyond 20%. After every oxidation experiment, the resultant product was analyzed via XRD to determine the phases present. For as-fabricated samples, Figure 7 confirms the presence of terminal-oxide UO_2 phase in the completed experiments (above) with the arrested experiments resulting in a distribution of U_3Si_2, $U_2Nb_3Si_4$, $U_{2-x}Nb_{3+x}Si_4$, and UO_2.

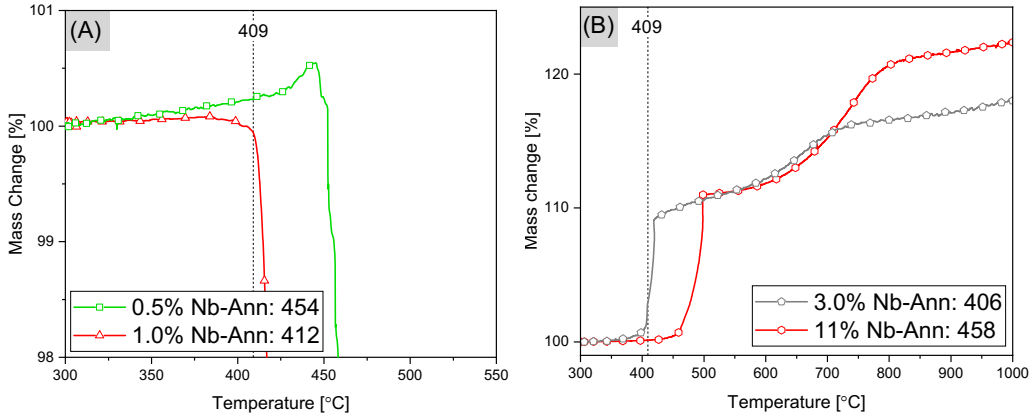

Figure 6. Thermogravimetric plots of selected annealed compositions oxidized in steam and ramped to 1000 °C. In each plot, the composition is labeled by its respective vol % Nb concentration and its oxidation onset temperature. I.e.: the U_3Si_2 + 0.5 vol% Nb composition is the green trend with square points and had an onset temperature of 454 °C. (**A**) Arrested measurements; (**B**) Completed measurements.

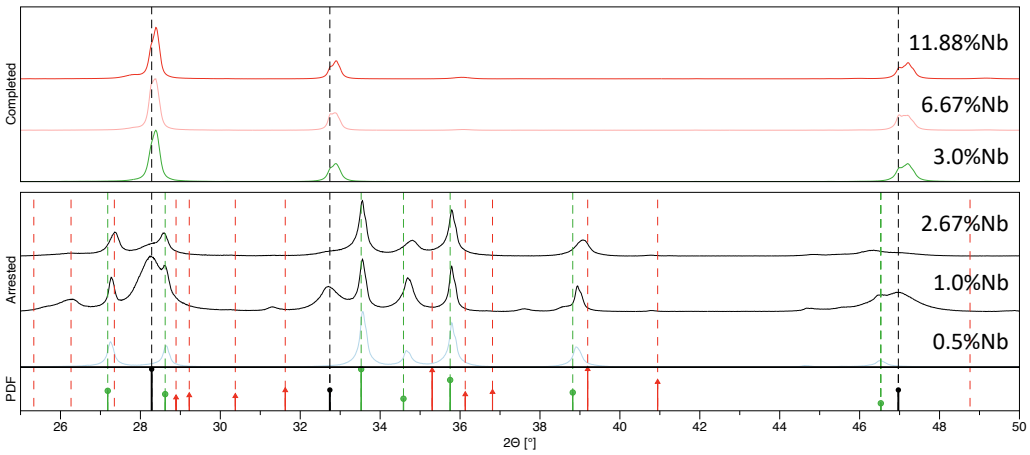

Figure 7. XRD results of the oxidation product of as-fabricated U_3Si_2 + Nb fragments. Arrested patterns display the multiple phases present, including U_3Si_2 (green circles, 01-075-1941), $U_2Nb_3Si_4$ (red triangle, 04-018-5866), $U_{2-x}Nb_{3+x}Si_4$ (04-019-6232), and UO_2 (black circle, 00-004-1422). Completed patterns agree with shifted UO_2.

4. Discussion

4.1. Comparison of As-Fabricated Analysis

Microstructures of the as-fabricated and annealed samples show distinct differences and are discussed in terms of the known thermodynamic investigations available in the literature. Recall from Section 2.3 that the 11.88 vol% Nb composition was annealed at 725 °C for 100 h. This temperature was selected as a representative of typical intermediate LWR fuel temperatures. A preliminary analysis of the 11.8 vol% Nb sample confirmed a phase evolution and suggested that an increased temperature and duration might further influence the compositions toward equilibrium and better match the annealing parameters presented in Lebihan et al.'s paper [29]. The remaining samples were subsequently annealed at 950 °C for 200 h based on evidence of microstructural evolution at 725 °C.The following discussion compares samples up to 6.67 vol% Nb to the 1000 °C section of the ternary phase diagram while the 11.88 vol% Nb compares to the 850 °C section.

For visualization, each sample's Nb content is represented by a star or pentagon along the line joining U_3Si_2 and pure Nb, as shown in Figure 8, where 0.5–6.6 vol% Nb compositions are in the 1000 °C section and 11.8 vol% Nb is in the 850 °C section. At 1000 °C, equilibrated compositions should exhibit a three-phase distribution containing

U_3Si_2, $U_2Nb_3Si_4$, and a U-Si composition, as shown in Figure 8. Here, the U-Si phase most closely matches the eutectic identified by Okatmoto as 91 at% U-Si that melts at 985 °C [20]. Table 2 reports the predicted phase abundances for each sample as calculated by the lever rule from isothermal sections of phase diagrams available in Lebihan et al.'s work [29]. Then, actual abundances of as-fabricated samples are compared to these predicted quantities. SEM and XRD analyses of the as-fabricated ingots identified medium-gray U_3Si_2, dark-gray $U_2Nb_3Si_4$, and bright high U phases, as predicted. Compared to the predicted abundances in Table 2, quantities of each phase determined from SEM images show excess amounts of the U-Si eutectic. This excess is attributed to the non-equilibrium rapid cooling at the end of arc melting preferentially solidifying U_3Si_2 and U_2NbSi, with the remaining U-rich phase forming last. After heat treatment, changes in phase abundances for 0.5 and 1.0 vol% Nb show minimal changes in U_3Si_2 and the absence of the 91 at% U-Si phase. The U-rich phase is considered to have been redistributed into U_3Si_2. The XRD patterns confirm U_3Si_2 as the dominant phase and show minimal-to-no 2θ shift as Nb increases, suggesting that Nb is not accommodated within the U_3Si_2 tetragonal structure. $U_2Nb_3Si_4$ that is identified in XRD exhibits a shift to the lower angle in both as-fabricated and annealed samples, indicating an increase in lattice parameter. This could be due to the insolubility of Nb at these concentrations coupled with slow reaction kinetics during fast cooling and heating events.

Table 2. Volume percent phase abundance as predicted by 850 °C and 1000 °C sections of the U-Nb-Si ternary phase diagrams. ImageJ was used to calculate percentage by the lever rule. The 850 °C section was used for 11.88 vol% Nb composition only.

Nb Concentration	% U_3Si_2 Phase 1	% $U_2Nb_3Si_4$ Phase 2	% U-Si Eut. Phase 3	% U_3Si Phase 4	% $U_{2-x}Nb_{3+x}Si_4$ Phase 5
0.5%	97.00	1.9	1.10	0.00	0.00
1.0%	92.75	4.50	2.75	0.00	0.00
2.6%	85.68	8.94	5.38	0.00	0.00
3.0%	83.34	10.41	6.25	0.00	0.00
6.6%	64.55	22.22	13.23	0.00	0.00
11.88%	14.33	39.15	0.00	46.52	0.00

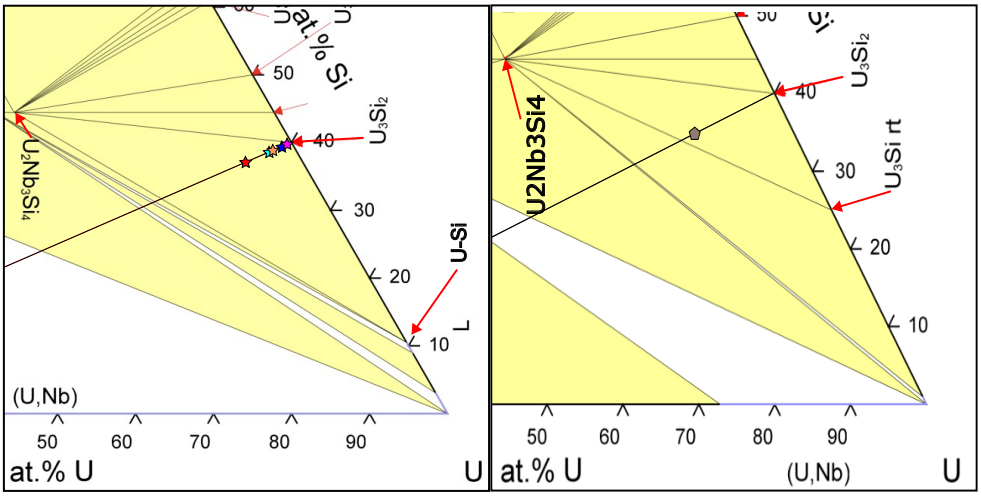

Figure 8. On the left, a selected area of the 1000 °C U-Nb-Si ternary phase diagram. The 0.5 (red) to 6.67 vol% Nb compositions are indicated by stars increasing in Nb concentration from right to left. A selected area of the 850 °C section of U-Nb-Si phase diagram is on the right. The 11.88 vol% Nb composition is indicated by a pentagon within the U_3Si_2, $U_2Nb_3Si_4$, and U_3Si phase areas. A solid line joining U_3Si_2 and pure Nb also indicates where proposed Nb compositions fall within the phase diagram.

The trend of secondary $U_2Nb_3Si_4$ and the U-Si phases distributed in a U_3Si_2 matrix phase persists at the intermediate concentrations of Nb, 2.6 and 3.0 vol%, but similarities end there. Annealed forms of these samples showed a notable decrease in U_3Si_2 abundance. Although the presence of U_3Si in the as-fabricated 1.0 and 2.6% Nb ingots was low, annealed forms showed an increase to 9.4 and 6.5% U_3Si relative areas, also suggesting that thermodynamic equilibrium has not been achieved but the composition is trending in this way. The $U_2Nb_3Si_4$ phase abundances are anomalous in that for 2.6% Nb, the predicted abundance of 8.9% was actually observed to be 6.8% in the annealed sample. This was a decrease from the as-fabricated 8.6%, which was closer to the predicted value. At 3.0% Nb, the predicted 10.5% abundance was observed as 6.3% in as-cast and increased up to 18.9% in the annealed. XRD phase peak locations did not shift within detection limits in U_3Si_2, showing minimal solubility in U_3Si_2 while the $U_2Nb_3Si_4$ phase peaks shifted to lower angles in $U_2Nb_3Si_4$, reinforcing agreement with Lebihan and the hypothesis that the annealing of the arc-melted ingots would result in compositions closer to an equilibrium phase distribution. Of particular significance at these Nb concentrations is the abundance of the 91 at% U-Si phase. Consultation of the U-Si binary phase diagram shows low melting temperatures for the U-Si eutectic at 985 °C. For fuels that would experience high pellet core temperatures, this low-melt phase could induce failure of the fuel before other phases would melt.

The last concentrations, 6.67 vol% Nb and 11.88 vol% Nb from Figure 8, display a phase evolution with the highest percent change for all phases as well as the formation of a second U-Nb-Si phase, initially identified as $U_{2-x}Nb_{3+x}Si_4$. Lebihan labels the only other ternary phase as $U_{1.75}Nb_{3.25}Si_4$; however, the SEM analysis here could not match this stoichiometry. It is hypothesized that despite a lack of EDS confirmation and agreement with the visual morphology description in the literature, this is $U_{1.75}Nb_{3.25}Si_4$. When compared to the predicted abundances of phases, as-fabricated ingots showed the best alignment with the ternary sections in U_3Si_2 with overabundance in $U_2Nb_3Si_4$ and poor abundance in the predicted U-Si phase. After their respective heat treatment, U_3Si_2 was reduced to less than half of its predicted value, while $U_2Nb_3Si_4$ and U-Si were three times more abundant than predicted. The $U_{1.75}Nb_{3.25}Si_4$ was not predicted but may be the result of overabundance of high U-rich phases leaving Nb excess to form these U-Nb-Si phases. U_3Si_2 remains the dominant phase in both as-fabricated and annealed XRD patterns with a low angle shift of the $U_2Nb_3Si_4$ phase.

Overall, phase totals have evolved to more closely align with predicted phase abundances from the 850 °C and 1000 °C phase diagram sections. U_3Si_2 was the dominant phase with no 2θ shift, suggesting no Nb solubility but further showed a strained distribution of $U_2Nb_3Si_4$ through a shift to lower angles in XRD. Additionally, abundances and identification of exact phase quantities present is especially difficult. Phases like those in well-studied systems like U_3Si_2 have been thoroughly investigated by computational and crystallographic analysis methods to confirm the lattice parameters and crystal structure. This enables such materials to be included as reference patterns available in crystal-structured databases. In contrast, the XRD patterns for the U-Si-Nb have only been identified by one source and have not been confirmed by other techniques. Calculation of quantities via Rietveld analysis requires well-defined reference patterns. In the fuels discussed here, this is not easily achieved since such reference patterns do not exist. Conducting Rietveld analysis for an exact quantitative abundance calculation of phases present therefore falls outside the scope of this study. Therefore, abundances and identification of phases present in this study can be qualitative, at best. In addition to calculating abundances through Rietveld analysis, reference patterns for ternary U-Nb-Si phases would be used to quantify any shift in XRD pattern. For example, it can be inferred from the U_3Si_2 phase that 2θ shifting can indicate a strained crystal structure, especially in the as-fabricated samples due to the insolubility of Nb. Of great importance here is the overall effect of the addition of Nb and the fuel's oxidation resistance performance.

4.2. Comparison of Oxidation Performance of Alloyed U_3Si_2

Materials for oxidation tests were mechanically fractured from bulk, and representative fragments were used. However, mechanical fracturing could induce other internal fracturing, which in turn may decrease overall oxidation resistance by providing an increased surface area for oxidation. Although this is not optimal, the method remains viable for testing the overall material. Figure 9 shows U_3Si_2 alloyed fuels from the literature as a comparison of vol% addition to U_3Si_2 and their respective oxidation onset temperature. The Nb-bearing compositions of this study performed the best and show that the technique of additions to pure U_3Si_2 has progressively improved. Figure 9 also helps to visualize the following discussion.

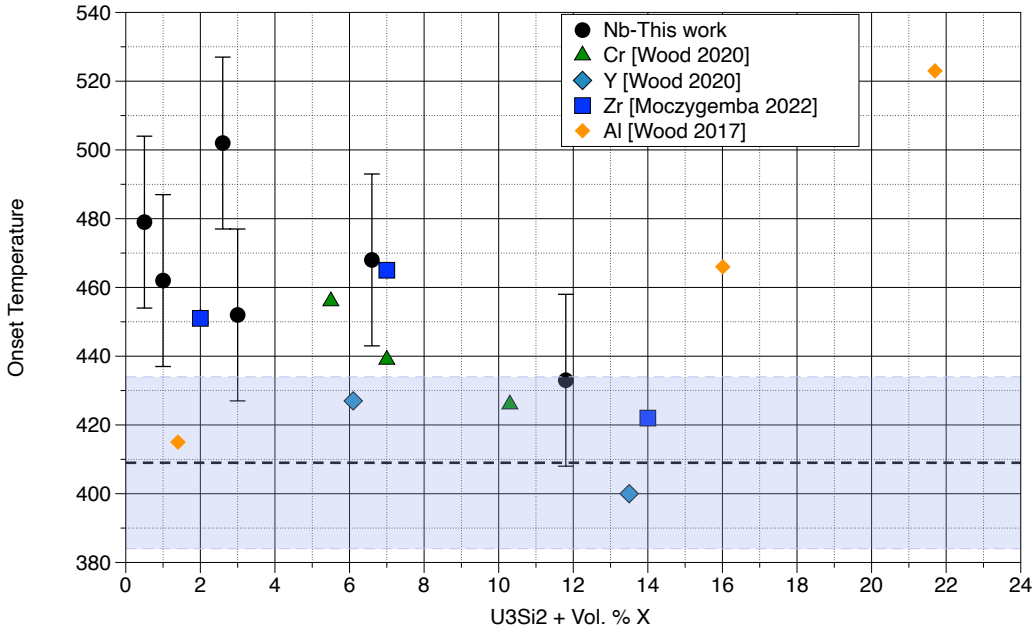

Figure 9. Comparison of U_3Si_2 alloyed with X (Nb, Cr, Y, and Zr) from the literature showing oxidation onset temperatures in high-temperature steam as a function of vol% X.

For as-fabricated ingots, oxidation onset improved the most from the 409 °C onset temperature of pure U_3Si_2. Of these ingots, the 2.6 vol% Nb composition exhibited the best oxidation onset temperature at 502.3 °C; however, it retained the characteristic U_3Si_2 two-part degradation mechanism, hydridization and oxidation, which led to energetic spallation and was consequently arrested. Since this is a primary degradation mechanism that Nb alloying sought to mitigate, the composition was not considered to have been successful. Therefore, of the completed compositions, the 3.0 vol% Nb composition exhibited the best performance. The onset of the 3.0 vol% composition was delayed to 451.7 °C and was coupled with the lowest total mass gain, 17% compared to 19% for 6.6 vol% Nb and 22% for 11.8 vol% Nb, over the duration of the experiment. Overall, the oxidation onset was delayed by less than 42.7 °C, relative to U_3Si_2. As shown in Figure 5A, the lower-concentration Nb compositions behaved the most like pure U_3Si_2 with an energetic mass ejection of the material from the experimental crucible. This matches the lower-concentration alloys of Al, Cr, Y, and Zr seen in previous studies [14]. When comparing pure U_3Si_2 to these U_3Si_2 + Nb fuels, a guiding hypothesis for this work was that the addition of the insoluble refractory Nb content would delay the onset of oxidation temperature. The delay in oxidation observed in the present work does lend itself to this theory and increased the fuel's resistance to cracking. Although identifying the exact method of mechanical strengthening was not a goal of this work, it is possible to postulate that increased interphase stress was able to decrease cracking, which in turn slowed oxidation. As the concentration of Nb increased for each composition, so did the number and abundance of secondary Nb-bearing phases.

Different and higher abundances of secondary phase could provide the stress gradient or defect sink necessary to stop or slow crack propagation through the fuel. An observed delayed onset of the oxidation temperature coupled with the decrease in mass gain further supports the effect. However, this cannot be quantitatively supported without first determining mechanical properties such as hardness or elasticity. Other investigations into the fuel could employ micro- or nano-indentation to obtain these values.

Despite a phase composition representative of a more thermodynamically equilibrated material, the annealed samples did not delay oxidation onset temperature further nor exhibit corrosion resistance greater than as-fabricated. In fact, the opposite is true. Oxidation performance displayed in Figure 6 exhibited mass gain with an onset temperature < 50 °C from the onset temperature of pure U_3Si_2 in Figure 6A. In terms of total mass gain when compared to the as-fabricated samples, the annealed samples surpassed 15% and peaked near 22%. Although a more homogeneous and stable phase distribution was achieved, heat treatment decreased the oxidation onset temperature (closer to pure U_3Si_2) and increased the total mass gain. When considering the potential for increased strength by adding Nb, it is believed that annealing decreased the stress available in the fuel to offset crack propagation. This is observed in Figure 6 as an overall decreased trend of oxidation onset temperature and increased mass gain. The hypothesis is further supported by Figures 2 and 4 in that the number and abundances of secondary phases is observed to decrease. Again, the mechanical properties of each phase would need to be measured quantitatively to determine the exact effect.

The performance of these compositions most closely resembled the response of U_3Si_2 alloyed with Cr and Y [14], wherein oxidation onset temperature of the compositions were delayed beyond that of pure U_3Si_2 while also affecting the total mass gain of the samples. When compared to those compositions, the use of Nb showed the best performance. When compared to the performance of Al-bearing U_3Si_2, the Nb-bearing material does not continue to improve as concentration increases beyond the U-loading required for the fuel to be viable in a drop-in replacement-type application.

For the compositions mentioned here, the Netzsch software c-DTA function was utilized. The function determines onset temperature by analyzing the rate of change in mass gain. However, a standard for this analysis has not been established in this field of study, particularly for nuclear fuels.

For energetically reactive materials like U_3Si_2, this lack of standard would prove problematic due to the low concentrations wherein the measurement was required to be halted from the energetic spallation of the material. This also brings fabrication methods and sample preparation for oxidation testing under consideration. The samples here were arc-melted, but materials in other studies that aimed to improve oxidation resistance were synthesized through conventional or spark plasma sintering, as listed and indicated in the literature reviews by Watkins and Gonzales [14,21]. From a material preparation perspective, a standard or convention would aid in minimizing measurement errors.

Despite the proposed high-temperature strength and corrosion benefits of adding niobium to U_3Si_2, the best performing composition, U_3Si_2 + 3.0 vol%, only increased the oxidation onset temperature by 42.7 °C. In addition to the temperature increase, this composition changed the two-part degradation mechanism to a degree that did not energetically expel material from the test crucible but did result in mass gain. At 3.0 vol% Nb, the fuel's overall mass gain is still problematic, especially in a sealed fuel pin assembly. Ultimately, these results suggest that the addition of a refractory material such as Nb to the U_3Si_2 fuel form did change its performance by delaying the onset temperature and reducing the energetic degradation of pure U_3Si_2 from spallation to simple mass gain.

5. Conclusions

Because of its use in other structural nuclear materials for strength and corrosion resistance, adding Nb to the accident-tolerant U_3Si_2 fuel candidate was proposed as an alloying method to improve oxidation performance over pure U_3Si_2. The phase distribution of the

as-fabricated and annealed results of the Nb-bearing composition was investigated in addition to high temperature, flowing steam, and oxidation testing designed to experimentally mimic conditions possible during off-normal reactor operations.

This work provides additional data on the behavior of Nb in the U_3Si_2 compound and finds that the as-fabricated compositions performed marginally better than their heat-treated counterparts. This is attributed to the formation of secondary Nb-rich phases causing further formations of U-rich phases. The phase segregation is hypothesized to diminish the delay in oxidation of U_3Si_2. These results are comparable to previous attempts of alloying U_3Si_2 with Al, Cr, Zr, and Y, wherein marginal delays in oxidation onsets were also observed. Performance improvements of U_3Si_2 + Nb fuel in water-bearing atmospheres was not significant; however, the technique offers promise. Should further investigation account for microstructural control by modifying the fabrication method, conventional pellet sintering, and other advanced sintering methods, the desired outcome could be achieved, especially in a more fully equilibrated system.

Author Contributions: Conceptualization, G.R., J.T.W. and E.S.S.; methodology, G.R.; formal analysis, G.R.; investigation, G.R.; resources, J.T.W. and E.S.S.; writing—original draft preparation, G.R.; writing—review and editing, G.R., J.T.W., S.W.P. and E.S.S.; visualization, G.R.; supervision, J.T.W., S.W.P. and E.S.S. All authors have read and agreed to the published version of the manuscript.

Funding: Initial support for the fabrication of these samples was provided by a Nuclear Regulatory Commission Faculty Development Grant titled: "Nuclear Fuels Research and Development Faculty Development Program at the University of Texas at San Antonio"; grant number (31310018M0046). Additional student support for characterization and analysis performed collaboratively among UTSA and LANL was supported by the CONNECT program, which operates under a National Nuclear Security Administration, Minority Serving Institution Partnership Program, grant award numbers DE-NA0002576 and DE-NA0004107. Student time and effort were supported by the Laboratory Directed Research and Development program of Los Alamos National Laboratory under Seaborg CR Project # 20210527CR.

Data Availability Statement: The raw data supporting the conclusions of this article will be made available by the authors on request.

Conflicts of Interest: The authors declare no conflicts of interest. The funders had no role in the design of the study; in the collection, analyses, or interpretation of data; in the writing of the manuscript; or in the decision to publish the results.

References

1. Costa, D.R.; Hedberg, M.; Middleburgh, S.C.; Wallenius, J.; Olsson, P.; Lopes, D.A. UN microspheres embedded in UO_2 matrix: An innovative accident tolerant fuel. *J. Nucl. Mater.* **2020**, *540*, 152355. [CrossRef]
2. Cappia, F.; Harp, J.M. Postirradiation examinations of low burnup U_3Si_2 fuel for light water reactor applications. *J. Nucl. Mater.* **2019**, *518*, 62–79. [CrossRef]
3. Wagner, A.R.; Harp, J.M.; Archibald, K.E.; Ashby, S.C.; Watkins, J.; Tolman, K.R. Fabrication of stoichiometric U_3Si_2 fuel pellets. *MethodsX* **2019**, *6*, 1252–1260. [CrossRef] [PubMed]
4. Zhou, W.; Zhou, W. Enhanced thermal conductivity accident tolerant fuels for improved reactor safety—A comprehensive review. *Ann. Nucl. Energy* **2018**, *119*, 66–86. [CrossRef]
5. Johnson, K.D.; Raftery, A.; Lopes, D.A.; Wallenius, J. Fabrication and Microstructural analysis of UN-U_3Si_2 composites for accident tolerant fuel applications. *J. Nucl. Mater.* **2016**, *477*, 18–23. [CrossRef]
6. Ortega, L.; Blamer, B.; Evans, J.; McDeavitt, S. Development of an accident-tolerant fuel composite from uranium mononitride (UN) and uranium sesquisilicide (U_3Si_2) with increased uranium loading. *J. Nucl. Mater.* **2016**, *471*, 116–121. [CrossRef]
7. Bragg-Sitton, S.M.; Todosow, M.; Montgomery, R.; Stanek, C.R.; Montgomery, R.; Carmack, W.J. Metrics for the Technical Performance Evaluation of Light Water Reactor Accident-Tolerant Fuel. *Nucl. Technol.* **2016**, *195*, 111–123. [CrossRef]
8. Yang, J.H.; Kim, D.J.; Kim, K.S.; Koo, Y.H. UO_2–UN composites with enhanced uranium density and thermal conductivity. *J. Nucl. Mater.* **2015**, *465*, 509–515. [CrossRef]
9. Harp, J.; Lessing, P.A.; Hoggan, R. Uranium Silicide pellet fabrication by powder metallurgy for accident tolerant fuel evaluation and irradiation. *J. Nucl. Mater.* **2015**, *466*, 728–738. [CrossRef]
10. Youinou, G.J.; Sen, R.S. Impact of accident-tolerant fuels and claddings on the overall fuesl cycle: A preliminary systems analysis. *Nucl. Technol.* **2014**, *188*, 123–138. [CrossRef]
11. Bragg-Sitton, S. Development of advanced accident-tolerant fuels for commercial LWRs. *Nucl. News* **2014**, *57*, 83.

12. Zinkle, S.; Terrani, K.; Gehin, J.; Ott, L.; Snead, L. Accident tolerant fuels for LWRs: A perspective. *J. Nucl. Mater.* **2014**, *448*, 374–379. [CrossRef]
13. Goldner, F. *Development Strategy for Advanced LWR Fuels with Enhanced Accident Tolerance*; Enhanced Accident Tolerant LWR Fuels National Metrics Workshop; U.S. Department of Energy: Washington, DC, USA, 12 June 2012.
14. Gonzales, A.; Watkins, J.K.; Wagner, A.R.; Jaques, B.J.; Sooby, E.S. Challenges and opportunities to alloyed and composite fuel architectures to mitigate high uranium density fuel oxidation: Uranium silicide. *J. Nucl. Mater.* **2021**, *533*, 153026. [CrossRef]
15. White, J.T.; Nelson, A.T.; Dunwoody, J.; Byler, D.; Safarik, D.; McClellan, K.J. Thermophysical Properties of U_3Si_2 to 1773 K. *J. Nucl. Mater.* **2015**, *464*, 275–280. [CrossRef]
16. Hastings, I. Burnup and temperature dependence of swelling in ǀceU3Si. *J. Nucl. Mater.* **1971**, *41*, 195–202. [CrossRef]
17. Hastings, I.; Stoute, R. Temperature-dependent swelling in irradiated ǀceU3Si fuel elements. *J. Nucl. Mater.* **1970**, *37*, 295–302. [CrossRef]
18. Bethune, B. Structural transformations in U_3Si. *J. Nucl. Mater.* **1969**, *31*, 197–202. [CrossRef]
19. Sooby Wood, E.; White, J.T.; Grote, C.; Nelson, A.T. U_3Si_2 behavior in H_2O: Part I, flowing steam and the effect of hydrogen. *J. Nucl. Mater.* **2018**, *501*, 404–412. [CrossRef]
20. Okamoto, H. Si-U (Silicon-Uranium). *J. Phase Equilibria Diffus.* **2013**, *34*, 167–168. [CrossRef]
21. Watkins, J.; Wagner, A.R.; Gonzales, A.; Jaques, B.J.; Sooby, E.S. Challenges and opportunities to alloyed and composite fuel architectures to mitigate high uranium density fuel oxidation: Uranium diboride and uranium carbide. *J. Nucl. Mater.* **2022**, *560*, 153502. [CrossRef]
22. Jaques, B.J.; Watkins, J.; Croteau, J.R.; Alanko, G.A.; Tyburska-Puschel, B.; Meyer, M.; Xu, P.; Lahoda, E.J.; Butt, D.P. Synthesis and sintering of UN-UO_2 fuel composites. *J. Nucl. Mater.* **2015**, *466*, 745–754. [CrossRef]
23. Kardoulaki, E.; Frazer, D.; White, J.T.; Carvajal, U.; Nelson, A.T.; Byler, D.D.; Saleh, T.; Gong, B.; Yao, T.; Lian, J.; et al. Fabrication and thermophysical properties of UO_2-UB_2 and UO_2-UB_4 composites sintered via spark plasma sintering. *J. Nucl. Mater.* **2021**, *544*, 152690. [CrossRef]
24. Turner, J.; Abram, T. Steam performance of UB_2/U_3Si_2 composite fuel pellets, compared to U_3Si_2 reference behaviour. *J. Nucl. Mater.* **2020**, *529*, 151919. . [CrossRef]
25. Turner, J. A high density composite fuel with integrated burnable absorber: U_3Si_2-UB_2. *J. Nucl. Mater.* **2020**, *529*, 151891. [CrossRef]
26. Gong, B.; Yao, T.; Lei, P.; Harp, J.M.; Nelson, A.T.; Lian, J. Spark plasma sintering (SPS) densified U_3Si_2 pellets: Microstructure control and enhanced mechanical and oxidation properties. *J. Alloys Compd.* **2020**, *825*, 154033. [CrossRef]
27. Snead, L.; Hoelzer, D.; Rieth, M.; Nemith, A. Chapter 13-Refractory alloys: Vanadium, Niobium, Molybdenum, Tungsten. In *Structural Alloys for Nuclear Energy Applications*; Elsevier: Boston, MA, USA, 2019. . [CrossRef]
28. Arblaster, J. The thermodynamic properties of Niobium. *J. Phase Equilibria Diffus.* **2017**, *38*, 707–722. . [CrossRef]
29. Lebihan, T.; Rogl, P.; Noel, H. The niobium-silicon-uranium system. *J. Phase Equilibria Diffus.* **2000**, *277*, 82–90. [CrossRef]
30. Wood, E.S.; Terrani, K.; Nelson, A. Sensitivity of measured steam oxidation kinetics to atmospheric control and impurities. *J. Nucl. Mater.* **2016**, *477*, 228–233. [CrossRef]